

# AERO-THERMAL ANALYSIS OF A REUSABLE LAUNCH VEHICLE DURING RE-ENTRY MANOEUVRER

A. Assonitis<sup>1</sup>, R. Paciorri<sup>1</sup>, V. Orlandini<sup>1</sup> & A. Neri<sup>2</sup>

<sup>1</sup>University of Rome "La Sapienza", Via Eudossiana 18, 00184 Rome, Italy <sup>2</sup>ESA ESRIN, Largo Galileo Galilei 1, 00044, Frascati, Italy

#### **Abstract**

The growing demand for space access, propelled by the continuous expansion of the space economy, stands as a primary motivator for the regain of interest for rockets re-usability. This paper aims at presenting the aero-thermal analysis of a simplified single-stage launch vehicle during both its ascent and descent path. In detail, 2D axis-symmetric computations were performed using the commercial gas-dynamic code CFD++ to predict the aerodynamic heating on the launch vehicle wall. Thermal loads were evaluated using a Conjugate Heat Transfer (CHT) technique, implemented in the CFD++ solver, which couples the fluid-dynamic field around the launch vehicle with the solid one within the launch vehicle walls. Furthermore, some considerations regarding surface heating due to the retropropulsion maneuver are drawn in this work.

Keywords: reusable launch vehicle, retro-propulsion, conjugate heat transfer, aero-thermal analysis

#### 1. Introduction

Reusable launch vehicles (RLVs) development represents an attractive field for space transportation market because it could significantly drive down launch costs [1, 2, 3, 4]. One of the most prominent examples of reusable launch vehicles is SpaceX Falcon 9 [5], a Vertical Takeoff Vertical Landing (VTVL) Two Stage To Orbit (TSTO) developed by SpaceX, which features a first stage that can return to Earth for vertical landings, enabling rapid refurbishment and reuse. However, the landscape of space launch continues to evolve rapidly. Many other companies and agencies are focusing on RLVs market and over the last decade are seeking to reach the same maturity level of SpaceX Falcon 9. As an example, DLR (Germany), CNES (France) and JAXA (Japan) are currently developing the CALLISTO demonstrator [6, 7], whereas many European researchers are working on the Horizon 2020 project RETALT[8, 9] to investigate launch system re-usability technologies of VTVL TSTO and SSTO RLV applying retro propulsion.

The recovery process of the reusable stages remains a severe technical challenge for the aerospace industry. One option is the use of retro propulsion [8], which consists in decelerating the vehicle during its return to ground by firing its engines. Although conceptually simple, this technique could cause significant sidewall heating, due to the hot exhaust plume that is deflected towards the launch vehicle surface by the external flow. The accurate estimation of thermal loads on reusable launch vehicles surface, and their consequent heating, during the entire trajectory is of paramount importance for designing a suitable thermal protection system. However, the magnitude of these heat fluxes are related to a variety of factors, such as the relative velocity between body and fluid, the engines operating time and, last but not least, the wall temperature and the material used for the launch vehicle walls [10]. This analysis cannot be owing to the expensive costs and limitations of ground-based testing for vehicles with propulsive hot jets, so it requires Computational Fluid Dynamics (CFD). In this framework, the proposed research aims to the evaluation of thermal loads during the descent of a single stage reusable launch vehicle, which decelerates via retropropulsion. It is organized as follows: Section 2. describes the numerical approach applied to compute thermo-fluid dynamic field around the launch vehicle. In detail, numerical simulations are carried out using the CFD++ [11] software of METACOMP, that applies a conjugate heat transfer approach [12] (CHT) to

couple the fluid-dynamic thermal field with the solid wall one. In Sect. 3a single-stage launch vehicle, used as benchmark for the proposed methodology, is presented: details on both the launch vehicle trajectories and on the nozzle flow modelling are also included in this Section. Key findings are summarized in Sect. 4. where numerical computations of both the ascent and the descent phases are discussed. Finally, future work activities are presented in the last Section.

## 2. Methodology: CFD solver and Conjugate Heat Transfer (CHT) technique

Numerical simulations are performed using Metacomp's commercial gasdynamic solver CFD++ [11], which is based on a finite volume discretization and it is second order accurate in time and space. In a finite volume method, the conservation equations, both of the solid and fluid phase in their integral form, are discretized directly in computational domain. In fact, the entire computation domain (fluid and solid) is divided into a finite number of small control cells, in each of which the integral equations written in discrete form are applied to evolve the averaged state of the wall. The solution to time t is given in terms of the average cell value of the vector of conservative variables. As previously stated, in this study we carried out CHT simulations using CFD++ code, where is also implemented a CHT solver based on a fully coupled technique [12]. In detail, both the fluid dynamic and the thermal fields in the solid are solved simultaneously, imposing the equality of the heat fluxes at the fluid/solid interface in every instant of the CHT simulation. For this reason, this method is suitable for non-stationary simulations. However, since numerical integration considers the same time intervals in both domains (the solid and the fluid one), it could be inefficient to consider the same time step during the numerical integration. For this reason, a careful assessment of the temporal integration parameters was carried out in order to ensure small numerical errors and reduced computation times.

Equations of both the fluid and solid phases are summarized hereafter:

### · Equations for fluid phase

Since the gas exiting the nozzle during retro-propulsion maneuver is composed by different species, the governing equations for a multi-species flow must be taken into account. However, the flow temperatures during the launch vehicle flight are not high enough to activate chemical reactions, so the flow around the launch vehicle is modeled as a non-reactive flow.

In detail, each component of the mixture satisfies the ideal gas equation using the Dalton's law:

$$p = \rho \bar{R}T$$

$$\bar{R} = R_0 \sum_{i} \frac{\sigma_i}{W_i} \tag{1}$$

where  $\rho$  the density, T the static temperature and  $R_0$  the universal gas constant. Moreover,  $\sigma_i$  and and  $W_i$  are the mass fraction and the molecular weight of the i-th specie, respectively. By defining  $c_{p_i}$  as the specific heat of i-th specie and  $\Delta H f_i$  the corresponding enthalpy of formation, the mixture enthalpy and internal energy are can be written as follows:

$$h = \sum_{i} \sigma_{i} \int_{-T}^{T} c_{p_{i}} dT + \sum_{i} \sigma_{i} \Delta H f_{i}$$
 (2)

$$e = \frac{p}{\gamma - 1} + \rho \frac{u^2 + v^2}{2} + \sum_{i=1}^{N} \rho \sigma_i \Delta H f_i$$
 (3)

where  $\gamma$  the ratio of specific heats for the mixture, which is obtained as:

$$\gamma = 1 + \frac{1}{\frac{\bar{c}_p}{R\sum_i(\sigma_i/W_i)} - 1} \tag{4}$$

with

$$\bar{c}_p = \frac{1}{T} \sum_i \sigma_i \int_T c_{p_i} dT \tag{5}$$

For 3D space, governing equations are expressed by Eq. 6:

$$\frac{\partial Q}{\partial t} + \frac{\partial}{\partial x}(F_1 + G_1) + \frac{\partial}{\partial y}(F_2 + G_2) + \frac{\partial}{\partial z}(F_3 + G_3) = \dot{S}$$
 (6)

where Q is the dependent variable vector;  $F_1$ ,  $F_2$  and  $F_3$  are the inviscid flux vectors;  $G_1$ ,  $G_2$  and  $G_3$  are the viscous flux vectors; and  $\dot{S}$  is the source term vector. These are given as:

$$\mathbf{Q} = \begin{pmatrix} e \\ \rho \\ \rho u \\ \rho v \\ \rho w \\ \rho \sigma_{1} \\ \vdots \\ \rho \sigma_{N-1} \end{pmatrix} \qquad \mathbf{F_{1}} = \begin{pmatrix} (e+p)u \\ \rho u \\ \rho u \\ \rho v u \\ \rho w u \\ \rho u \sigma_{1} \\ \vdots \\ \rho u \sigma_{N-1} \end{pmatrix} \qquad \mathbf{F_{2}} = \begin{pmatrix} (e+p)v \\ \rho v \\ \rho u v \\ \rho w v \\ \rho v w \\ \rho v \sigma_{1} \\ \vdots \\ \rho v \sigma_{N-1} \end{pmatrix} \qquad \mathbf{F_{3}} = \begin{pmatrix} (e+p)w \\ \rho w \\ \rho u w \\ \rho v w \\ \rho w v \\ \rho w \sigma_{1} \\ \vdots \\ \rho w \sigma_{N-1} \end{pmatrix} \qquad (7)$$

$$\mathbf{G_{1}} = \begin{pmatrix} \dot{q}_{x} - u\tau_{xx} - v\tau_{xy} - w\tau_{xz} \\ 0 \\ -\tau_{xx} \\ -\tau_{xy} \\ -\tau_{xz} \\ \rho D_{1,m} \frac{\partial \sigma_{1}}{\partial x} \\ \vdots \\ \rho D_{N-1,m} \frac{\partial \sigma_{N-1}}{\partial x} \end{pmatrix} \qquad \mathbf{G_{2}} = \begin{pmatrix} \dot{q}_{y} - u\tau_{yx} - v\tau_{yy} - w\tau_{yz} \\ 0 \\ -\tau_{yx} \\ -\tau_{yy} \\ -\tau_{yz} \\ \rho D_{1,m} \frac{\partial \sigma_{1}}{\partial y} \\ \vdots \\ \rho D_{N-1,m} \frac{\partial \sigma_{N-1}}{\partial x} \end{pmatrix} \qquad \mathbf{G_{3}} = \begin{pmatrix} \dot{q}_{z} - u\tau_{zx} - v\tau_{zy} - w\tau_{zz} \\ 0 \\ -\tau_{zx} \\ -\tau_{zy} \\ -\tau_{zz} \\ \rho D_{1,m} \frac{\partial \sigma_{1}}{\partial z} \\ \vdots \\ \rho D_{N-1,m} \frac{\partial \sigma_{N-1}}{\partial z} \end{pmatrix}$$

where e is the total energy,  $\rho$  is the density, p is the pressure, u, v and w are the velocity components in the x, y and z directions respectively and  $\sigma_i$  is the mass fraction of species i. The species diffusion terms are modeled using the species gradients and the molecular diffusion coefficient of the i-th specie in the mixture,  $D_{i,m}$ , which is computed under the assumption that the Schmidt number is constant (Sc = 0.7). For a Newtonian fluid, the stresses and strains are linearly related:

$$\tau_{xx} = 2(\mu + \mu_t) \frac{\partial u}{\partial x} - \frac{2}{3}(\mu + \mu_t)\phi$$

$$\tau_{yy} = 2(\mu + \mu_t) \frac{\partial v}{\partial y} - \frac{2}{3}(\mu + \mu_t)\phi$$

$$\tau_{zz} = 2(\mu + \mu_t) \frac{\partial w}{\partial z} - \frac{2}{3}(\mu + \mu_t)\phi$$

$$\tau_{xy} = \tau_{yx} = (\mu + \mu_t)(\frac{\partial u}{\partial y} + \frac{\partial v}{\partial x})$$

$$\tau_{xz} = \tau_{zx} = (\mu + \mu_t)(\frac{\partial u}{\partial z} + \frac{\partial w}{\partial x})$$

$$\tau_{yz} = \tau_{zy} = (\mu + \mu_t)(\frac{\partial v}{\partial z} + \frac{\partial w}{\partial y})$$

$$(8)$$

where  $\mu$  is the molecular viscosity of the mixture,  $\mu_t$  is the turbulent viscosity and  $\phi$  is the dilation given by:

$$\phi = (\frac{\partial u}{\partial x} + \frac{\partial v}{\partial y} + \frac{\partial w}{\partial z}) \tag{9}$$

From Fourier's law of conduction, we can write:

$$\dot{q}_x = -(k+k_t) \frac{\partial T}{\partial x}$$

$$\dot{q}_y = -(k+k_t) \frac{\partial T}{\partial y}$$

$$\dot{q}_z = -(k+k_t) \frac{\partial T}{\partial z}$$
(10)

where k is the thermal conductivity of the mixture and  $k_t$  is the turbulent thermal conductivity. In detail, molecular viscosity  $\mu$  and thermal conductivity k are obtained from Sutherland's law:

$$\frac{\mu}{\mu_{ref}} = \left(\frac{T}{T_{ref}}\right)^{1.5} \frac{T_{ref} + S_{\mu}}{T + S_{\mu}} \tag{11}$$

$$\frac{k}{k_{ref}} = \left(\frac{T}{T_{ref}}\right)^{1.5} \frac{T_{ref} + S_k}{T + S_k} \tag{12}$$

where the coefficients for each species are reported in Table 1.

	Air	CO	$CO_2$	$H_2O$
$T_{ref}$ [K]	273.16	273.16	273.16	273.16
$\mu_{ref} \left[ \frac{kg}{ms} \right]$	$1.716 \cdot 10^{-5}$	$1.65 \cdot 10^{-5}$	$1.38 \cdot 10^{-5}$	$1.00 \cdot 10^{-5}$
$k_{ref} \left[ \frac{W}{mK} \right]$	$2.41 \cdot 10^{-2}$	$2.31 \cdot 10^{-2}$	$1.46 \cdot 10^{-2}$	$1.61 \cdot 10^{-2}$
$S_{\mu}[K]$	111	102	253	523.3
$S_k[K]$	194	221.3	939.8	1276

Table 1 – Coefficients for the conductivity and viscosity functions for each specie.

By posing the turbulent Prandlt number  $(Pr_t)$  equal to 0.9, we are able to determine the turbulent thermal conductivity  $k_t$  as follows:

$$k_t = \frac{\mu_t c_p}{P r_t} \tag{13}$$

The turbulent viscosity  $\mu_t$  is calculated using the Spalart-Allmaras (SA) model [13], which provides a variable  $\tilde{v}$  through the following differential equation:

$$\frac{\partial}{\partial x_i}(u_j\tilde{v}) = c_{b1}f_{r1}(1 - f_{t2})\tilde{S}\tilde{v} + \frac{1}{\sigma}(\nabla \cdot ((v + \tilde{v})\nabla\tilde{v}) + c_{b2}(\nabla\tilde{v})^2) - \left(c_{w1}f_w - \frac{c_{b1}}{\kappa^2}f_{t2}\right)\left(\frac{\tilde{v}}{d}\right)^2 + f_{t1}\Delta U^2.$$
 (14)

The turbulent kinematic viscosity  $v_t$  is obtained from the variable  $\tilde{v}$  by means of

$$v_t = \tilde{v} f_{v1} \tag{15}$$

where  $f_{v1}$ ,  $f_{t1}$ ,  $f_{t2}$ ,  $f_w$ ,  $f_{t2}$  and  $f_{r1}$  are dumping functions and hence the turbulent viscosity be given by:

$$\mu_t = \bar{\rho} \nu_t \tag{16}$$

For the interested reader, the constants and functions used in the SA equation are reported in Ref. [13]. RANS equations are applied also to model launch vehicle flight in laminar regime. However, a negligible turbulent viscosity is imposed at infinite and the production term of Eq. 14 is deactivated in this case to match the Navier-Stokes equations.

## · Equations for solid phase

In the present study, the wall is modelled as an isotropic homogeneous solid material with the same density, thermal conductivity and specific heat in each point. Heat exchange is given by conduction within the solid material, without heat generation or absorption that could be provided by a possible cooling system. Therefore the temperature field in the solid phase is obtained by the Fourier equation:

$$\rho c_p \frac{\partial T}{\partial t} = k \nabla^2 T \tag{17}$$

To connect the thermal field of the solid wall with that of the flow-field, the equality of the thermal fluxes at the solid/fluid interface is imposed.

$$k_f \frac{\partial T}{\partial n} \bigg|_{f} = k_s \frac{\partial T}{\partial n} \bigg|_{s} \tag{18}$$

where  $k_f$  and  $k_s$  are the thermal conductivities of the solid phase and of the fluid phase and  $\frac{\partial T}{\partial n}\Big|_f$  and  $\frac{\partial T}{\partial n}\Big|_s$  are the temperature gradients calculated at the interface in the fluid phase and in the solid phase, respectively.

#### 3. Test-case definition

The simplified smooth launch vehicle displayed in Fig. 1 is considered to test the methodology proposed in Sect. 2.so that the effect of protrusions (side ducts, antennas, grid fins etc) is neglected. Figure 1 points out the characteristic launch vehicle dimensions including also the diameter of the nozzle exit section, which are chosen in similarity with the first stage of the reusable launch vehicle in Ref.[14]. To evaluate the aerodynamic heating of this launch vehicle, its surface is modelled using a 1 cm thick layer of aluminum (see Tab. 2 for details on the material properties), initially at ambient temperature (298 K).

Table 2 – Aluminum properties [15] for the single-stage launch vehicle in Fig. 1.

Thickness	Density	Sp. Heat	Th. Cond.
cm	kg/m3	J/KgK	W/mK
1	2810	960	155

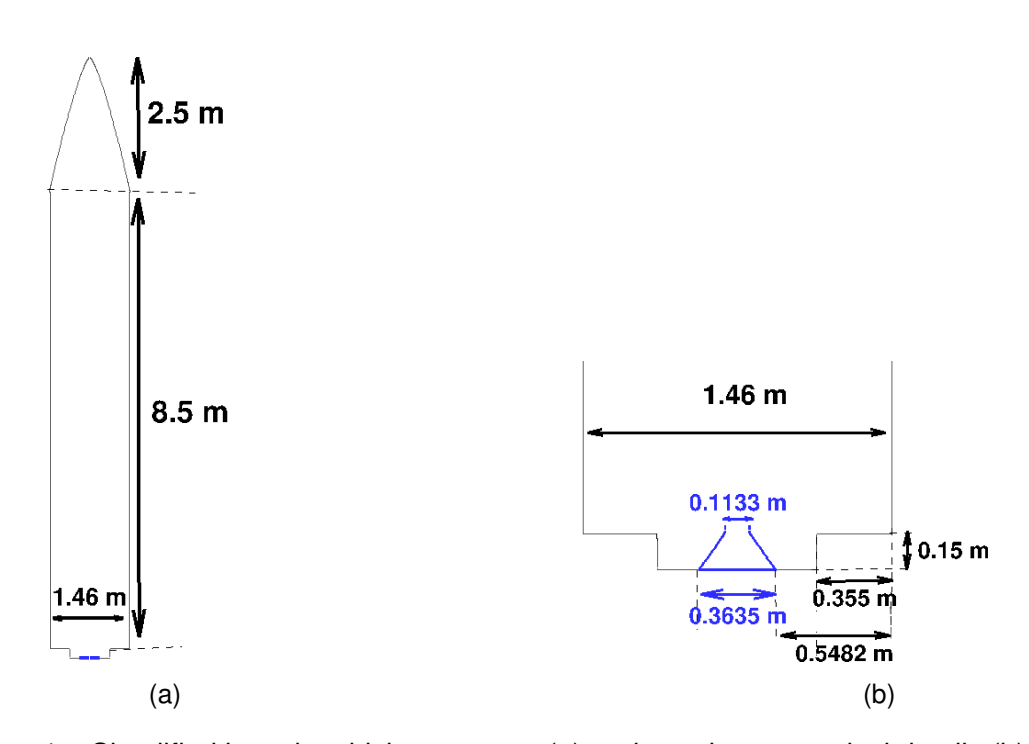


Figure 1 – Simplified launch vehicle geometry (a) and nozzle geometrical details (b).

Assuming zero angle-of-attack, the ascent and the descent phases can be computed by performing 2D axis-symmetric simulations on the two computational domains plotted in Fig. 2, which are discretized by the multi-block structured grids in Figs. 3 and 4.

Some considerations must be drawn regarding the definition of computational domain, since the domain external boundary must take into account the different flight conditions during the ascent/descent path. First of all, the inlet boundary (blue edges in Fig. 2) must be placed sufficiently far from the launch vehicle fairing, so that the detached shock in front of the space launch vehicle is always contained in the computational domain. Moreover, also the upper side boundaries (marked in green in Fig. 2) must be located sufficiently far from the launch vehicle walls to avoid that the shock waves forming within the flow-field reflect on these boundaries. This requirement is of paramount importance especially when  $M_{\infty}$  is relatively small (for instance  $M_{\infty} = 1.5$ ), because in these conditions, the angles formed by the shock waves w.r.t. the free-stream direction are large. Finally, as in the ascent phase the exhaust gas exiting the nozzle does not

play any role in the launch vehicle wall heating, the nozzle is not included in the ascent domain. Similarly, the fairing is not included in the descent domain since we interested in evaluating the wall temperature increase only on the launch vehicle sidewalls.

Grids details are reported for both the ascent and descent domain in Tabs. 3 and 4, respectively. Indeed, these tables summarize the number of blocks, the number of nodes and the minimum/maximum element size  $\Delta s$  used in each block.

Figure 2 describes also the specific boundary conditions imposed in each case: smaller frames of this figure provide details on the launch vehicle wall modeling using the CHT technique in Sect. 2. By varying in time the free-stream conditions in the inlet section, depicted using a solid blue line in Fig. 2, it is possible to simulate the flow-field around the launch vehicle during both the ascent and the descent trajectories. It is worth noting that the nozzle is only included in the computational domain used for the descent phase, in order to evaluate also the thermal loads due to retro-propulsion.

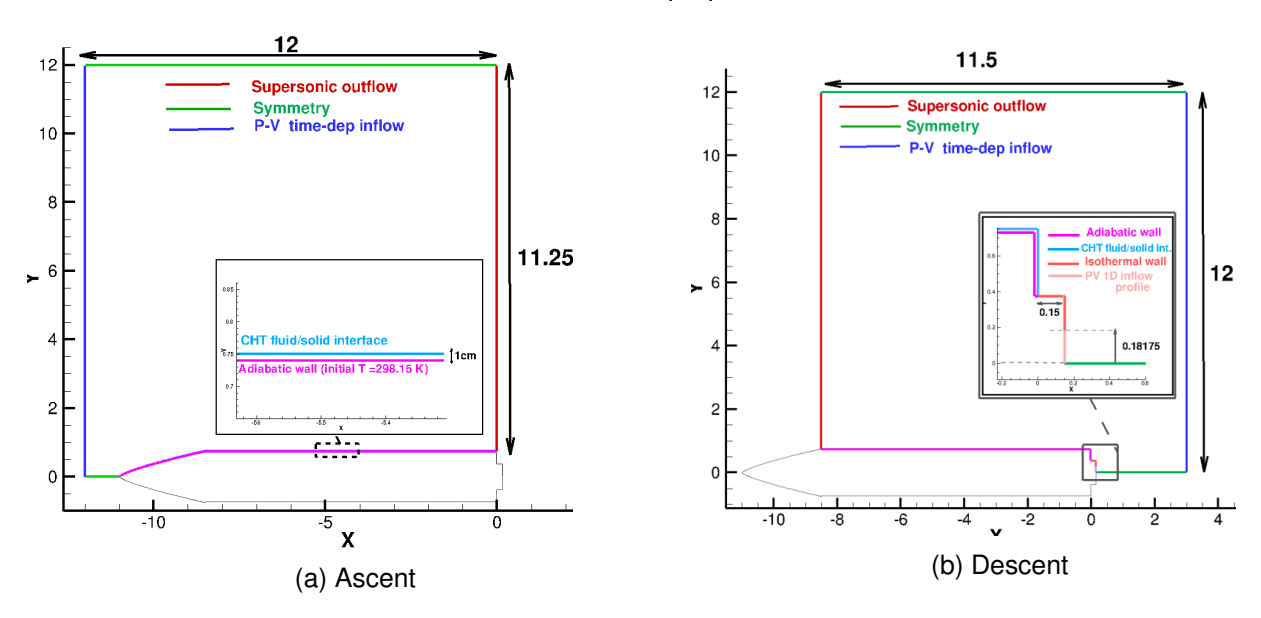


Figure 2 – Computational domain and prescribed boundary conditions

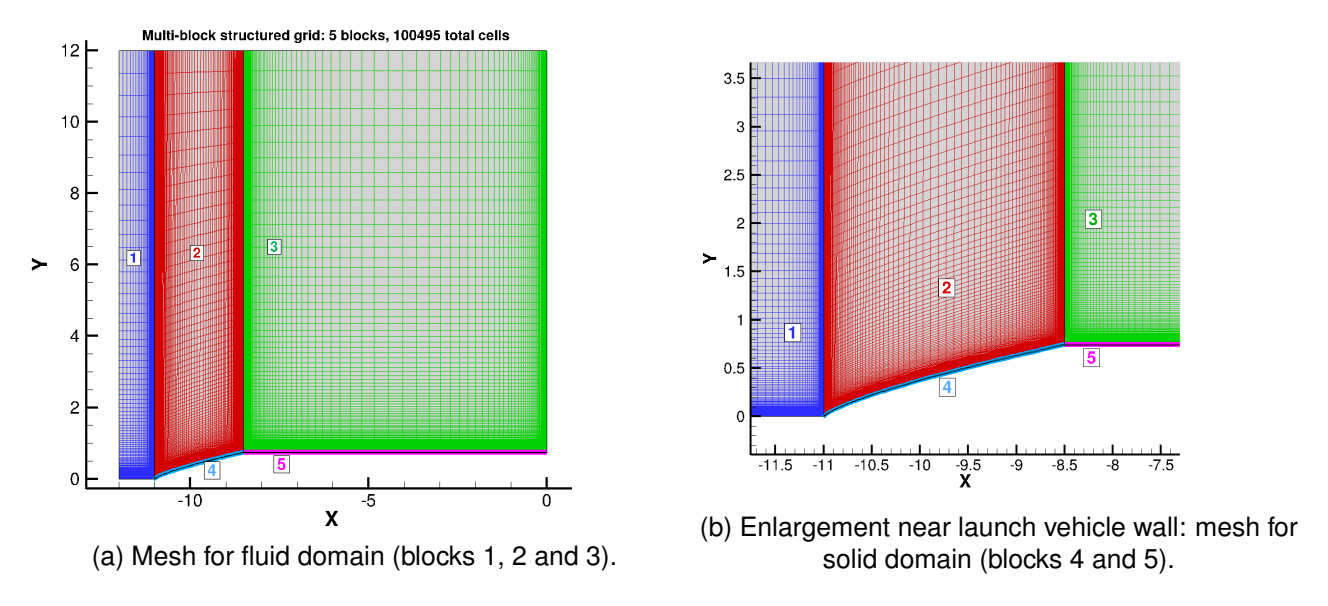


Figure 3 – Ascent phase. Multi-block structured grid: each block is marked by a different color.

Block	Nodes	$\Delta s_{min}$ (m)	$\Delta s_{max}$ (m)	Domain
1	40x200	$10^{-5}$	0.65	fluid
2	200x200	$10^{-5}$	0.65	fluid
3	200x200	$2.00 \cdot 10^{-5}$	0.57	fluid
4	200x35	$10^{-5}$	0.05	solid
5	200x35	$2.00 \cdot 10^{-5}$	0.38	solid
	Total cells:	100495		

Table 3 – Ascent phase. Multi-block structured grids details

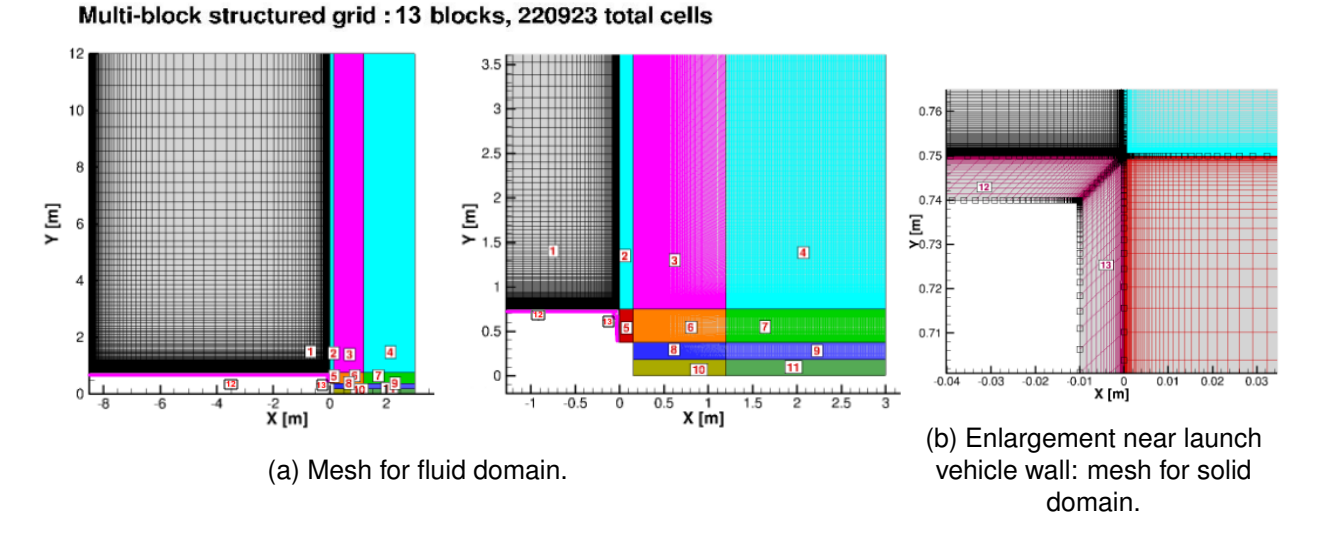


Figure 4 – Descent phase. Multi-block structured grid: each block is marked by a different colour.

# 3.1 Ascent/Descent Trajectories

The following seven equations of motion (Eq. 19) are required to determine the ascent/descent trajectories of the single-stage launch vehicle in Fig. 1.

$$\begin{cases} \dot{\vec{r}} = \vec{v} \\ \dot{m} = -\frac{T}{I_{sp}g_0} \\ \dot{\vec{v}} = \frac{\vec{F}_g}{m} + \frac{\vec{D}}{m} + \frac{\vec{T}}{m} \end{cases}$$
(19)

In detail, an oxygen/methane rocket engine is taken into account, as the one described in Ref. [16]. Similarly to Ref. [14], a total mass of 3 tons is considered for the simplified launch vehicle in Fig. 1. Besides, the following assumptions were considered:

• Rocket thrust (T) Rocket thrust was expressed as:

$$T = (T_{vac} - p_a A_e) \tag{20}$$

where  $T_{vac}$  is the vacuum thrust and  $I_{sp}$  the specific impulse. The atmospheric pressure at certain altitude  $p_a$  is computed from Earth GRAM model [17], whereas the nozzle area at exit  $A_e$  is derived from data in Fig. 1b.

• **Drag (D)** Under the assumption of zero angle-of-attack, the drag (D) is the only aerodynamic force:

$$D = \frac{1}{2}\rho C_D S v^2 \tag{21}$$

Block	Nodes	$\Delta s_{min}$ (m)	$\Delta s_{max}$ (m)	Domain
1	200x200	$2.00 \cdot 10^{-5}$	0.57	fluid
2	100x200	$2.00 \cdot 10^{-5}$	0.57	fluid
3	200x200	$2.00 \cdot 10^{-5}$	0.57	fluid
4	200x200	$2.00 \cdot 10^{-4}$	0.42	fluid
5	100x200	$2.00 \cdot 10^{-5}$	0.025	fluid
6	200x200	$2.00 \cdot 10^{-4}$	0.015	fluid
7	200x100	$2.00 \cdot 10^{-5}$	0.015	fluid
8	200x100	$2.00 \cdot 10^{-4}$	0.009	fluid
9	200x30	$2.00 \cdot 10^{-5}$	0.009	fluid
10	200x30	$2.00 \cdot 10^{-4}$	0.009	fluid
11	200x30	0.006	0.009	fluid
12	200x35	$2.00 \cdot 10^{-5}$	0.38	solid
13	35x100	$2.00 \cdot 10^{-5}$	0.025	solid
	Total cells:	220923		

Table 4 – Descent phase. Multi-block structured grids details

where the atmospheric density  $\rho$  is provided by the Earth GRAM model [17] and S is the launch vehicle cross-section. Drag coefficient  $C_D$  is expressed as Mach function by performing several steady CFD simulation at free-stream Mach number ranging from 0.5 to 4.

Under the aforementioned assumptions, it is possible to compute the launch vehicle ascent and the descent trajectories, which are respectively plotted in Figs. 5 and 6 in terms of Mach vs altitude and Reynolds vs Mach, where Reynolds number was computed using the launch vehicle height (11 m) as reference length. It can be observed from Fig. 5b that Reynolds number diminishes as the altitude increase. In detail, it varies from  $10^8$  to  $10^7$  during the ascent propulsive phase, and therefore turbulent flow can be assumed in this phase, whereas a laminar regime can be considered during the ballistic ascent.

Similar consideration can be drawn for the descent phase. By evaluating the Reynolds vs Mach number trend in Fig. 6b, Re increases throughout the descent trajectory. Indeed, for Reynolds values smaller than  $10^6$  up to  $M_{\infty}=3$ , it is reasonable to consider laminar flow during the first stage of the descent, while for higher values of the Reynolds number the launch vehicle flight is characterised by turbulent flow regime. Regarding the retro-propulsion modelling, the engine was supposed to be activated at 28 km altitude for around 20s, in similarity with Ref. [18].

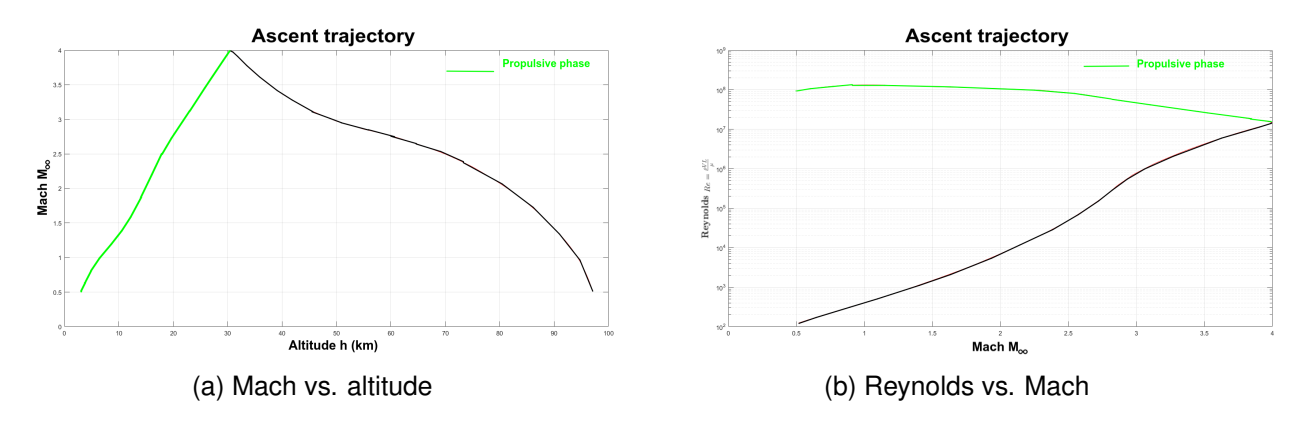


Figure 5 – Ascent trajectory

#### 3.2 Rocket exhaust gas modeling and nozzle flow simulation

To evaluate the retro-propulsion effect during the descent path, it is necessary to model the exhaust gas exiting the nozzle. Indeed, flow variables profile extracted from the nozzle exit section must be provided as inflow in the computational domain in Fig. 2b, as shown by the enlargement around the nozzle in

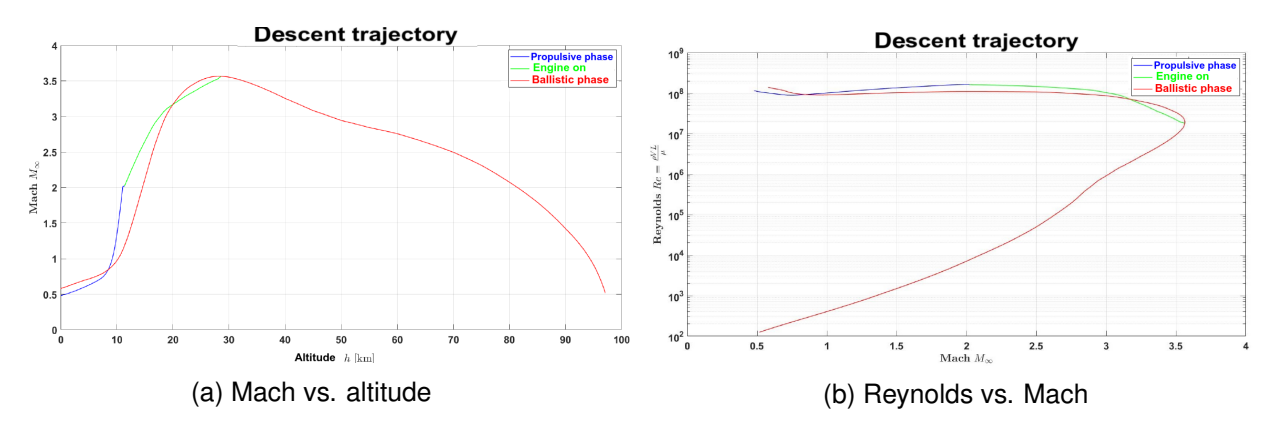


Figure 6 – Descent trajectory

this figure. Therefore, information regarding the nozzle geometry and the engine operating regime are required. In detail, nozzle is assumed to be conical, with a half cone angle of 35 degrees and an area ratio  $(A_e/A_t)$ , i.e. the ratio of the nozzle exit area and throat area, equal to 10.29 (see Fig. 1b). Combustion chambers conditions are set as in Ref. [16]  $(T_0 = 3600 \text{ K})$  and  $p_0 = 60 \text{ bar}$ . For retro-propulsion maneuver, we assumed that the engine provides 60% thrust, so that the chamber pressure is set equal to  $p_0 = 38 \text{ bar}$ . By providing the total pressure, propellants mixture ratio and the nozzle expansion ratio to CEA program, developed by NASA [19], it is possible to compute flow conditions at nozzle throat. At this point, a 2D axisymmetrical numerical simulation of the nozzle divergent section can be performed using CFD++, where the flow variables profile computed by CEA is imposed as inflow condition. Moreover, gas composition provided by CEA is frozen in the divergent section. The computational domain used for the nozzle flow simulation is sketched in Fig. 7a, which describes also the prescribed boundary conditions. Figure 7b shows the computed pressure flow-field. Flow variables distribution at the exit section (see Fig. 8) is extracted from the CFD solution and provided as inflow profile to model the gas coming out of the rocket engine during retro-propulsion.

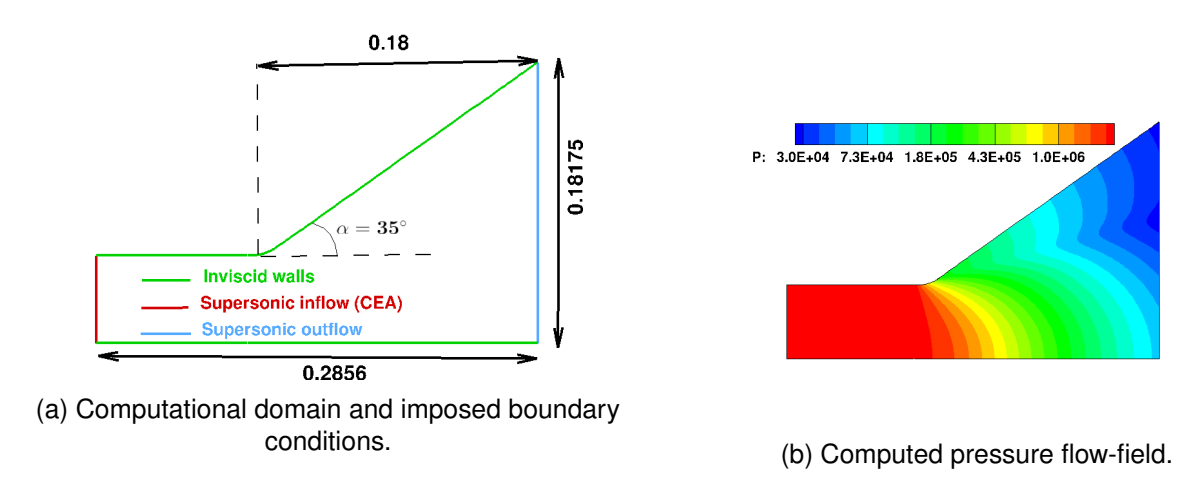


Figure 7 – Conical nozzle

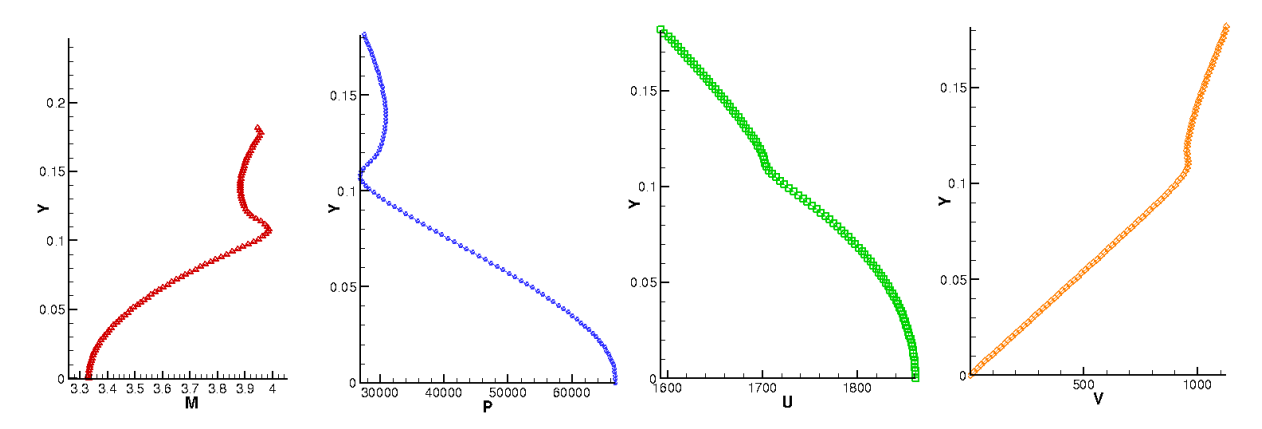


Figure 8 – Flow variables profile extracted from nozzle exit section.

#### 4. Results

#### 4.1 Ascent phase

To estimate the wall temperature distribution during the descent, the effect of the aerodynamic heating during the ascent phase must be taken into account. Since aerodynamic heating causes the increase of the vehicle wall temperature, it is reasonable to expect that the temperature reached at the end of the ascent trajectory would be different from the value imposed at the beginning of the flight.

Ascent phase was computed by performing 2D axis-symmetric simulations on the computational grid in Fig. 3. Spalart-Allmaras model [13] was used to account for turbulence. In detail, ascent simulation starts from 27s after launch vehicle liftoff, corresponding to 11.6 km altitude and to  $M_{\infty} = 1.5$  free-stream Mach number, and it ends when the launch vehicle reaches 89km altitude. It is not the maximum altitude reached by the launch vehicle (97 km): however, this simulation concerns the supersonic flight phase where  $M_{\infty} \geq 1.5$ , since in this phase aerodynamic heating has the major effect on the launch vehicle structures. To consider aerodynamic heating effect during the early stage of the ascent (t < 27s), 10 K wall temperature increase w.r.t. the initial value was assumed (298.5K).

Figure 9 shows the Mach flow-field evolution during the ascent phase in some trajectory points, marked with different colored symbols in the last frame (i). This figure highlights the effect of the velocity variation on the Mach angles and shock slopes: moreover, it can be observed the boundary layer thickening as altitude increases.

Figure 10 plots the wall temperature variation ( $\Delta T$ ) on the launch vehicle surface at the end of the ascent phase: temperature rises by around 5-7 K w.r.t. the initial value imposed at the beginning of the ascent simulation (308.15 K), except for the launch vehicle fairing where temperature increase is significantly higher. Figure 11 details the launch vehicle surface heating by focusing on the wall point at x = 4.45m, marked by a red circle in Fig. 10. Specifically, the wall temperature growth and the heat flux variation in time are plotted in Fig. 11 a and 11b, respectively. The latter figure points out that heat flux reaches a maximum value around time t = 25s, corresponding approximately to 10 km altitude, and then it tends to zero. During the ascent early phase, the free-stream Mach number rises, whereas the external temperature decrease. When the free-stream temperature approaches a value around 200 K, and in the meantime the Mach number still increases, wall temperature rises to 314 K (40° C), then it keeps constant until the end of the ascent.

#### 4.2 Ballistic descent

Two different computations were performed to simulate the launch vehicle descent phase, depending on whether the rocket engine is powered on. In this Subsection, results corresponding to the case of the ballistic descent (red trajectories in Fig. 6), where retro-propulsion is not applied, are reported.

Descent simulation started at 89 km altitude and  $M_{\infty}=1.52$ . To account for the aerodynamic heating during the coasting phase, which is not simulated, the wall temperature reached at the end of the ascent phase is further increased by 30 K to be conservative. As noted in Subsect. 3.1 a transition between laminar/turbulent flow occurs during the descent phase. Since it cannot be exactly predicted when the transition occurs, we impose the transition at to different Reynolds number values:  $Re = 5 \cdot 10^6$  and  $Re = 10^7$ ,

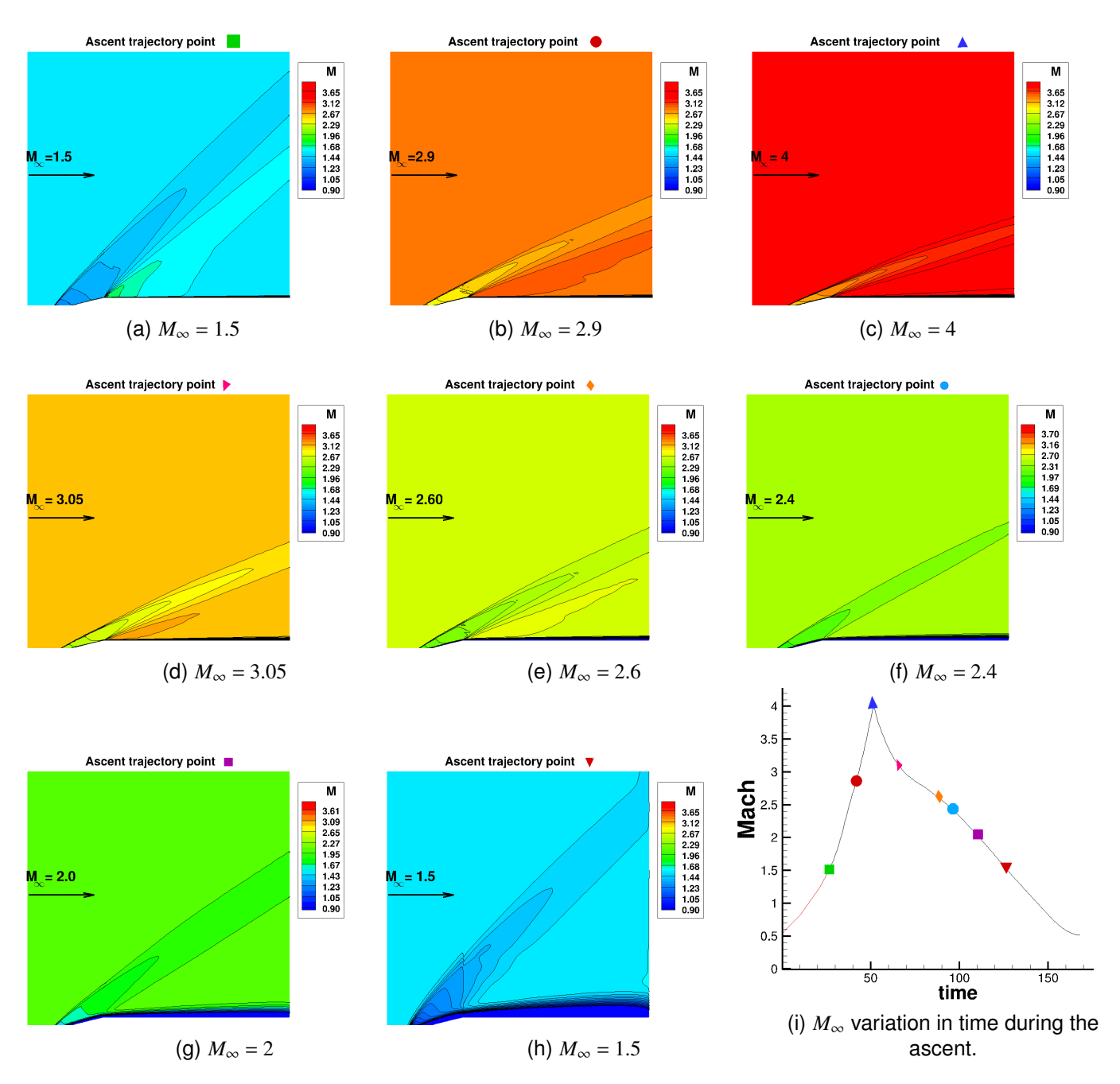


Figure 9 – Ascent phase: Mach flow-field evolution (a-h) in the trajectory points marked in frame (i)

corresponding to respectively 71 s and 75 s from the beginning of the ballistic descent simulation.

Mach flow-field evolution during the descent is shown by frames from 12a to 12h. These figures highlight that boundary layer becomes thinner as the altitude decreases. Moreover, since during the descent the Mach number initially increases and then decreases, the slope of the oblique shocks and the shock layer thickness vary accordingly.

Concerning the launch vehicle surface heating at the end of the descent, wall temperature increase along the cylinder sidewalls does not exceed 10 K. More information regarding the temperature growth during the flight can be obtained by focusing on a precise point placed on the launch vehicle surface, as done in Fig. 11 for the ascent phase. Squared symbols in Fig. 14 describes both the temperature and the heat flux variation in time for the point at X = 4.45 m, circled in red in Fig. 13. It can be noted that temperature is approximately constant until the transition to turbulent flow takes place (t = 71s): when turbulence model is activated, heat flux sharply increases and as consequence, wall temperature varies from 343.15 K (descent initial value) to approximately 349 K. To evaluate the effect of a delayed laminar/turbulent transition,

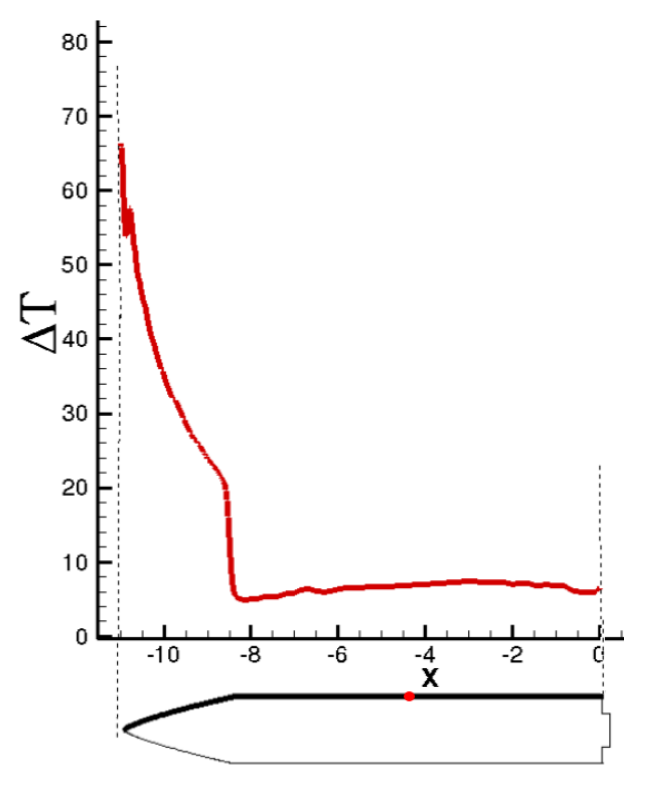


Figure 10 – Wall temperature increase (K) due to aerodynamic heating

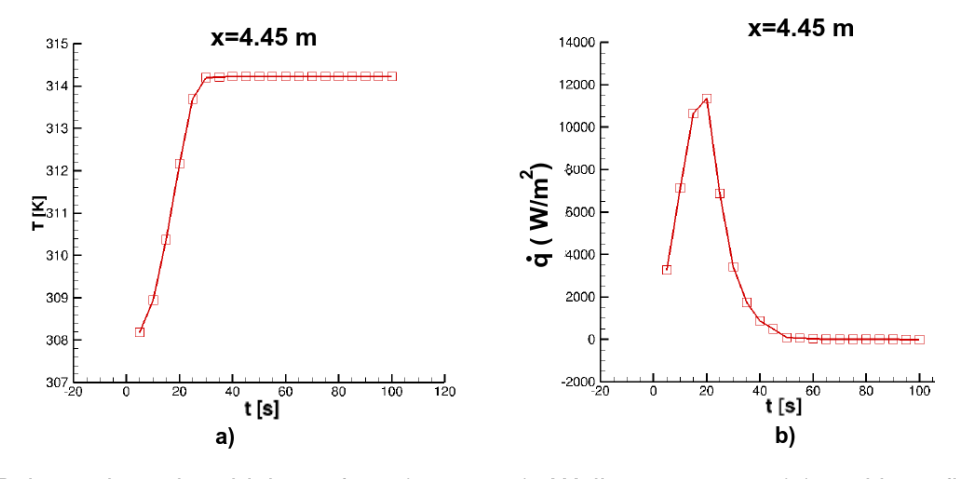


Figure 11 – Point on launch vehicle surface (x=4.45m). Wall temperature (a) and heat flux (b) values during ascent

ballistic descent was also computed by imposing the laminar/turbulent transition at  $Re = 10^7$  (75s from the descent beginning). In this case, the results in terms of the wall temperature and heat flux distributions (triangular blue symbols in Fig. 14) are almost superimposed to those obtained when laminar/turbulent transition is set at t = 71s.

## 4.3 Descent phase with retro-propulsion manoeuvre

To simulate the retro-propulsion manoeuvre, the rocket engine was activated for 20 s when the launch vehicle reaches 28km altitude, approximately at  $t=78\,s$  from the beginning of the descent, when flight Mach number is around  $M_{\infty}=3.55$ . Exhaust gas conditions are provided by a preliminary CFD++ computation, as described in SubSect. 3.2and are imposed as 1D inflow profile at nozzle exit section. Moreover, since Reynolds number is above  $10^7$  during this flight phase, fully developed turbulent flow was considered. To provide a qualitative estimate of the launch vehicle surface heating during retro-propulsion, Fig. 15a-15e show the temperature flow-field evolution when the rocket engine is activated. In each frame, it can be noted not only the bow shock originating in the launch vehicle after-body region, but also the shock

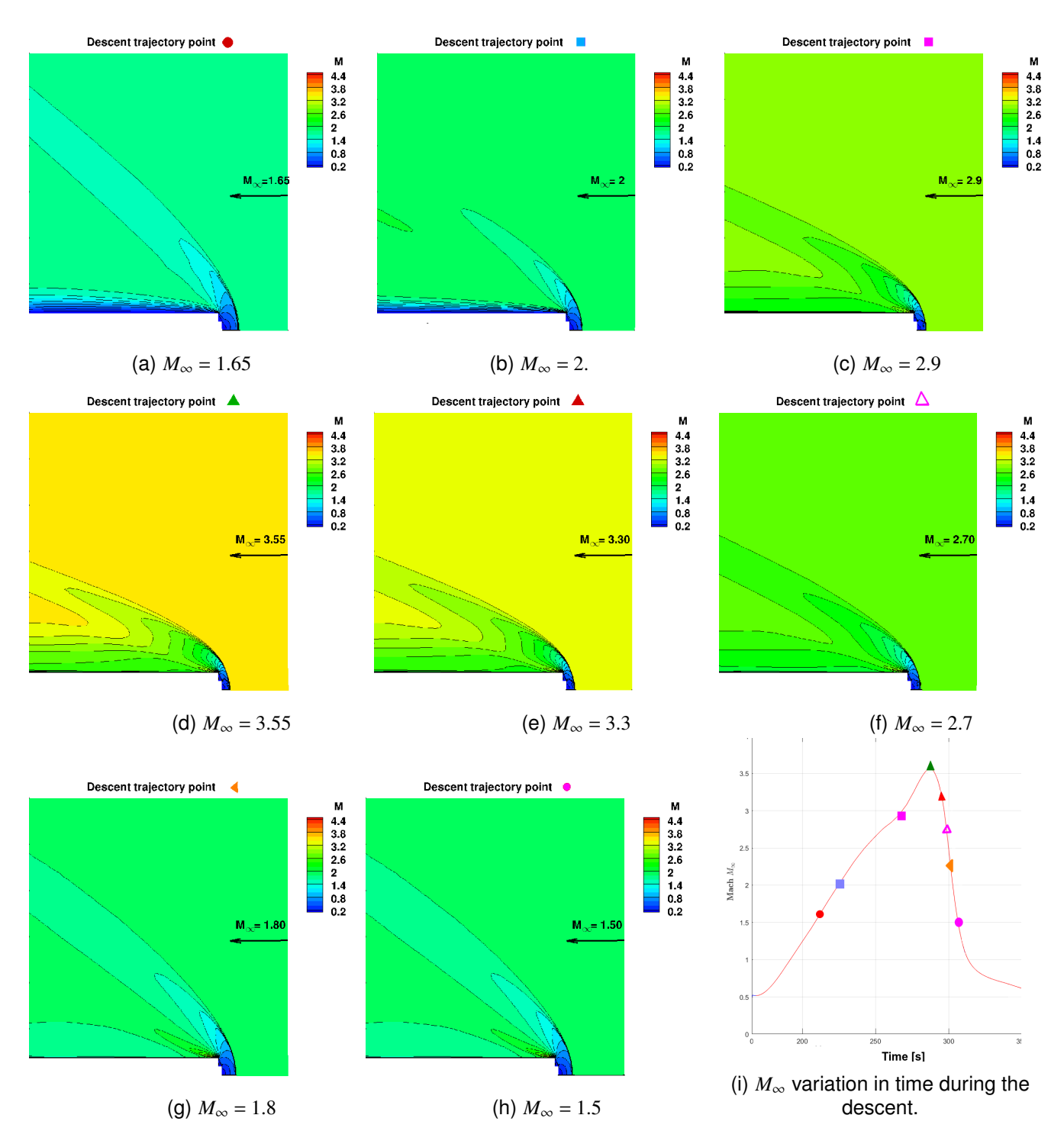


Figure 12 – Ballistic descent: Mach flow-field evolution (a-h) in the trajectory points marked in frame (i)

pattern due to the interaction of the hot exhaust plumes with the subsonic flow downstream the bow shock. This flight phase is strongly unsteady due to the presence of two shocks: the former makes subsonic the nozzle jet, whereas the latter decelerates the external stream. Thermal loads on launch vehicle surface are mainly affected by this interaction: the plume flow is forced to turn so that launch vehicle walls are fully immersed in the hot exhaust gas, featuring temperature values higher than 2000 K as illustrated in Fig. 16. Figure 18 makes evident the heating of vehicle walls caused by retro-propulsion: while the rocket engine fires, temperature at x = 4.45m (circled point in Fig. 17) increases well beyond the maximum allowable temperature for the aluminum alloy ( $T_{max} = 90^{\circ}C$ ). Temperature starts decreasing when the engine is turned off. Even if a conservative high value was set for the descent initial temperature, Figures 17 and 18 point

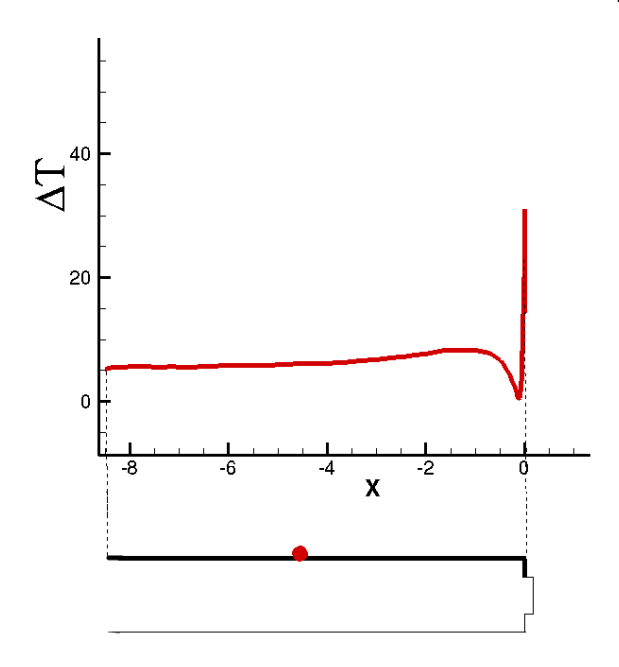


Figure 13 – Wall temperature increase (K) due to aerodynamic heating

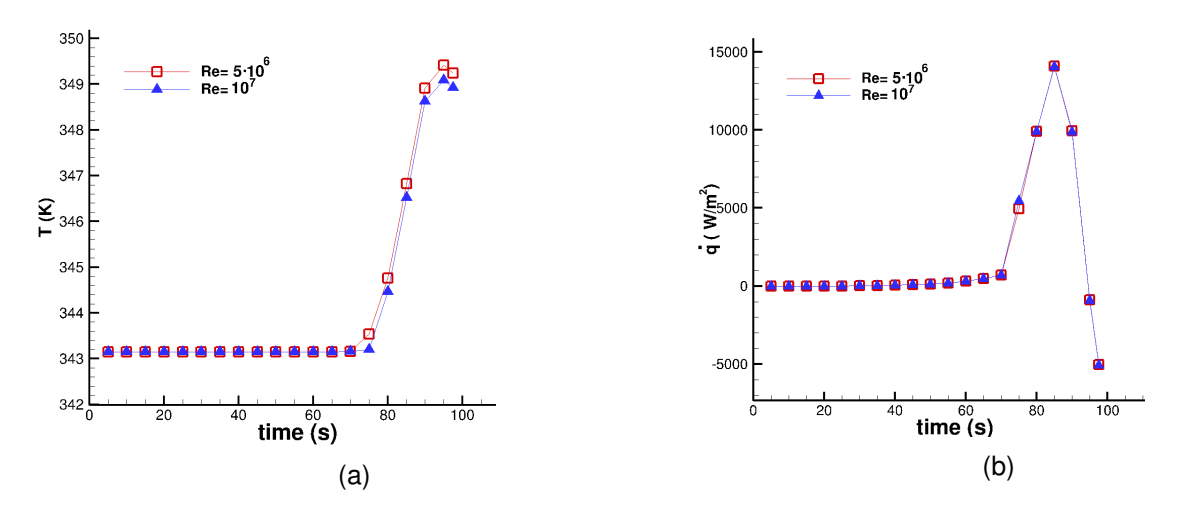


Figure 14 – Point on launch vehicle surface (x=4.45m). Wall temperature (a) and heat flux (b) values during ballistic descent.

out that retro-propulsion causes significant sidewall heat loads, due to the effect of the hot exhaust plume on the launch vehicle surface. To prevent damages to the launch vehicle structures, thermal protections could be required. Alternatively, a contained temperature rise can be achieved by reducing the rocket engine ignition time to less than 10 s.

#### 5. Conclusions and future work

This work aims to study a reusable launch vehicle descent flight phase, with special emphasis to the aerothermal effects owing to a retro-propulsion maneuver. In detail, it focuses on both the description of the methodology applied to carry out this task and on the definition of a simplified single-stage launch vehicle, considered as a benchmark for our approach. 2D axis-symmetric computations of both the launch vehicle ascent and the descent flight phases were performed using the commercial gas-dynamic code CFD++ and the CHT technique implemented in this solver to evaluate thermal loads acting on the launch vehicle walls. While aerodynamic heating during ascent and ballistic descent causes a slight rise of surface temperature, numerical simulations of the retro-propulsion maneuver predict significant heating of the launch vehicle, since wall temperatures are well beyond the maximum allowable temperature of the material.

Future work will focus on the definition of a more realistic test-case to better understand the retro-propulsion effects on reusable stages. At this regard, also 3D simulations will be performed to study the effect of non

#### **INSERT RUNNING TITLE HERE**

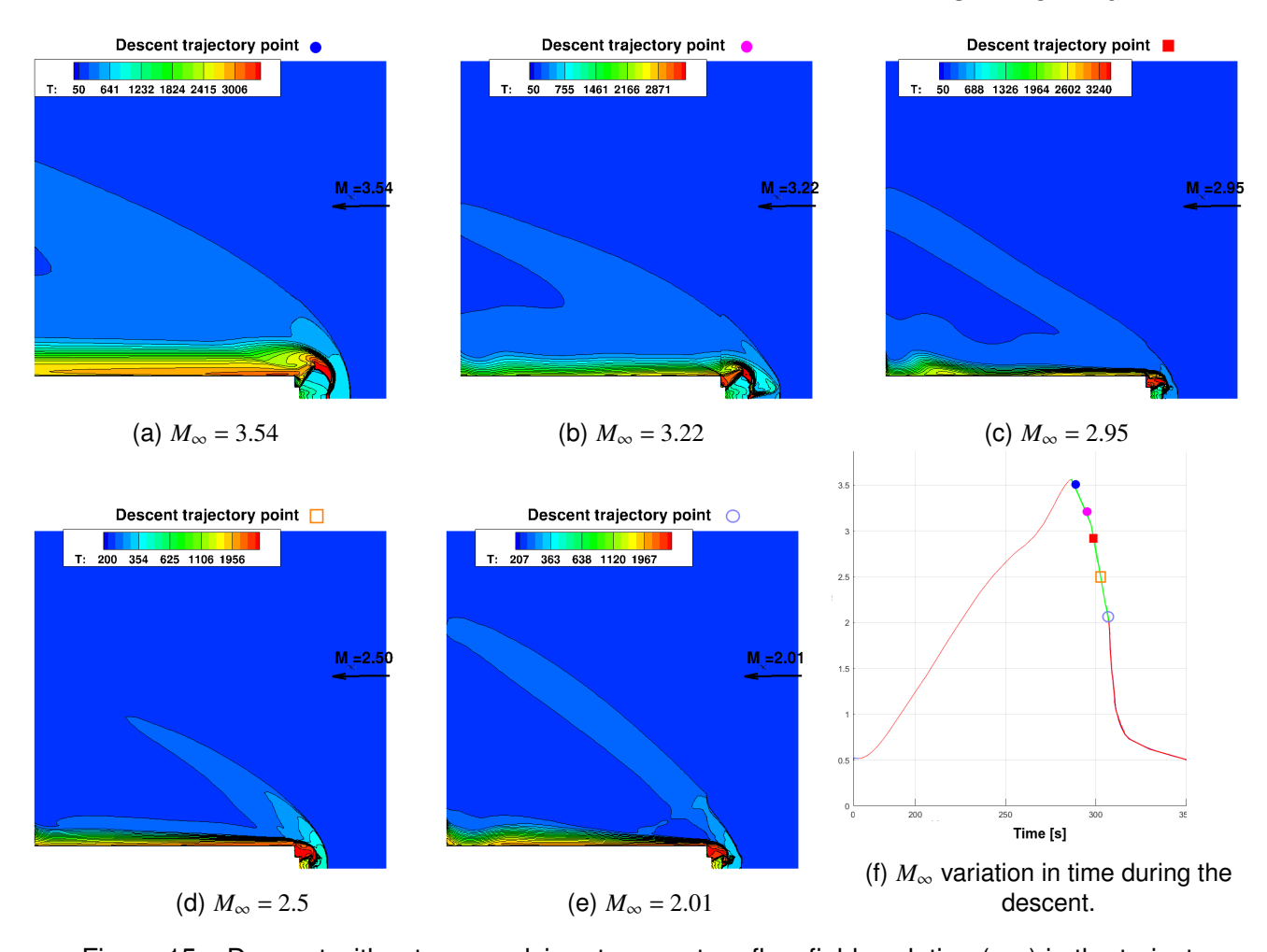


Figure 15 – Descent with retro-propulsion: temperature flow-field evolution (a-e) in the trajectory points marked in frame (f)

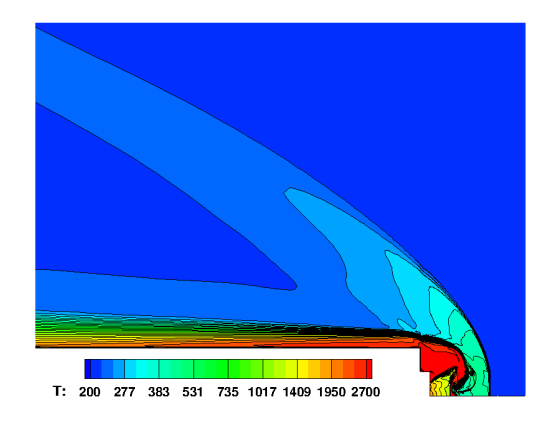
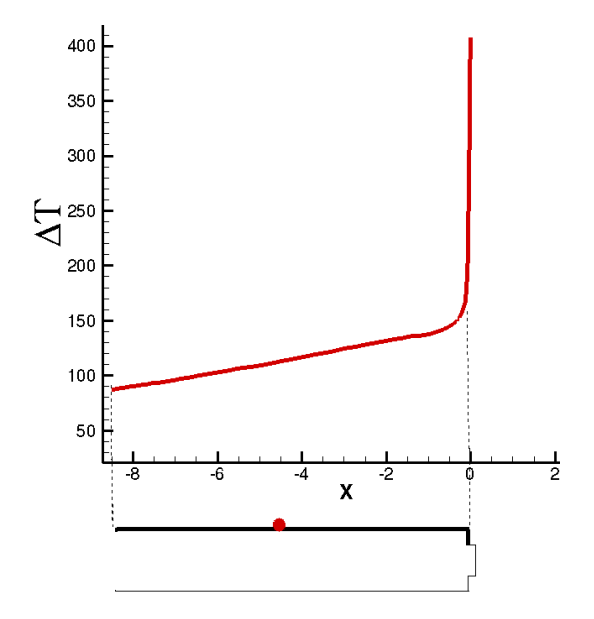


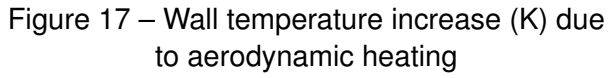
Figure 16 – Enlargement of Fig.15d around launch vehicle walls.

zero angle-of-attack during launch vehicle flight as well as to evaluate the aerodynamic heating on the launch vehicle protrusions, as in Ref.[20, 21].

## 6. Acknowledgements

This research is jointly funded by Sapienza University and the European Space Agency as a part of ESA Contract No. 4000141038/23/IT/RAS.





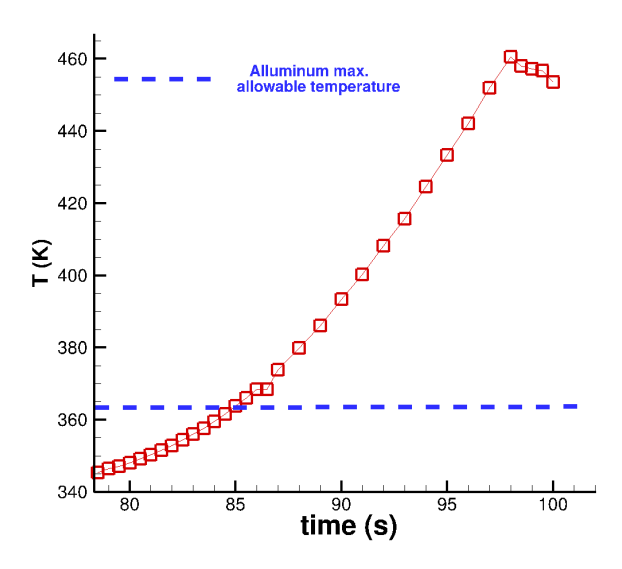


Figure 18 – Point on launch vehicle surface (x=4.45m). Wall temperature values during descent.

# 7. Copyright Statement

The authors confirm that they, and/or their company or organization, hold copyright on all of the original material included in this paper. The authors also confirm that they have obtained permission, from the copyright holder of any third party material included in this paper, to publish it as part of their paper. The authors confirm that they give permission, or have obtained permission from the copyright holder of this paper, for the publication and distribution of this paper as part of the ICAS proceedings or as individual off-prints from the proceedings.

#### References

- [1] Mohamed Ragab and F McNeil Cheatwood. Launch vehicle recovery and reuse. In AIAA Space 2015 Conference and Exposition, page 4490, 2015.
- [2] Richard Webb. Is it worth it?-the economics of reusable space transportation. In *International Cost Estimating and Analysis Association (ICEAA) 2016 International Training Symposium*, number M16-5593-1, 2016.
- [3] Paolo Baiocco. Overview of reusable space systems with a look to technology aspects. *Acta Astronautica*, 189:10–25, 2021.
- [4] Guillermo J Dominguez Calabuig, Miraux Loïs, Andrew Ross Wilson, Alberto Sarritzu, Angelo Pasini, et al. Eco-design of future reusable launchers: insight into their life-cycle and atmospheric impact. In *Proceedings* of the 9th European Conference for Aeronautics and Space Sciences. EUCASS (European Conference for AeroSpace Sciences), 2022.
- [5] SpaceX (Ed.). Falcon user's guide, 2020.
- [6] Etienne Dumont, Shinji Ishimoto, Pascal Tatiossian, Josef Klevanski, Bodo Reimann, Tobias Ecker, Lars Witte, Johannes Riehmer, Marco Sagliano, Sofia Giagkozoglou Vincenzino, et al. Callisto: a demonstrator for reusable launcher key technologies. *Transactions of the Japan Society for Aeronautical and Space Sciences, Aerospace Technology Japan*, 19(1):106–115, 2021.
- [7] Etienne Dumont, Svenja Woicke, Marco Sagliano, Adrian Krieger, Sven Krummen, Steffen Callsen, Malte Stief, Kevin Bergmann, Aaron Koch, Markus Markgraf, et al. Callisto reusable rocket stage demonstrator: consolidating the design. In 2024 IEEE Aerospace Conference, pages 1–19. IEEE, 2024.
- [8] Ansgar Marwege, Josef Klevanski, Johannes Riehmer, Daniel Kirchheck, Sebastian Karl, Davide Bonetti, J Vos, Matthew Jevons, Anett Krammer, and João Carvalho. Retro propulsion assisted landing technologies (retalt): Current status and outlook of the eu funded project on reusable launch vehicles. 2019.
- [9] Mariasole Laureti and Sebastian Karl. Aerothermal databases and load predictions for retro propulsion-assisted launch vehicles (retalt). *CEAS Space Journal*, 14, 2022.
- [10] John David Anderson. Hypersonic and high-temperature gas dynamics second edition. *American Institute of Aeronautics and Astronautics*, 2006.

- [11] Sukumar Chakravarthy, Oshin Peroomian, Uriel Goldberg, and Sampath Palaniswamy. The cfd++ computational fluid dynamics software suite. In AIAA and SAE, 1998 World Aviation Conference, page 5564, 1998.
- [12] Bibin John, P Senthilkumar, and Sreeja Sadasivan. Applied and theoretical aspects of conjugate heat transfer analysis: A review. *Archives of Computational Methods in Engineering*, 26(2):475–489, 2019.
- [13] P.R. Spalart and S.R. Allmaras. One-equation turbulence model for aerodynamic flows. *Recherche aerospatiale*, (1):5–21, 1994. cited By 2038.
- [14] Pedro Simplicio, Andres Marcos, and Samir Bennani. A reusable launcher benchmark with advanced recovery guidance. In 5th CEAS Conference on Guidance, Navigation & Control, 2019.
- [15] Asm aerospace specification metals inc.
- [16] Victor P. Zhukov. The impact of methane oxidation kinetics on a rocket nozzle flow. *Acta Astronautica*, 161:524–530, 2019.
- [17] PW White and J Hoffman. Earth global reference atmospheric model (earth-gram): User guide. Technical report, 2023.
- [18] Tobias Ecker, Franziska Zilker, Etienne Dumont, Sebastian Karl, and Klaus Hannemann. Aerothermal analysis of reusable launcher systems during retro-propulsion reentry and landing. 2018.
- [19] Bonnie J McBride. Computer program for calculation of complex chemical equilibrium compositions and applications, volume 2. NASA Lewis Research Center, 1996.
- [20] A Di Mascio, S Zaghi, R Muscari, R Broglia, B Favini, and A Scaccia. On the aerodynamic heating of vega launcher: Compressible chimera navier–stokes simulation with complex surfaces. In 7th European Aerothermodynamics Symposium, Brugge, Belgium, pages 9–12, 2011.
- [21] M. Leopardi, R. Paciorri, A. Assonitis, A. Neri, and D. Barbagallo. Effects of protuberances on surface loads on the vega-c launch vehicle. *Journal of Spacecraft and Rockets*, 2024.